Contactless Power Supply for Magnetically Levitated Elevator Systems

Rüdiger Appunn, Aryanti K. Putri and Kay Hameyer

Institute of Electrical Machines, RWTH Aachen University, Aachen, Germany
Ruediger.appunn@iem.rwth-aachen.de

Abstract

In a modern, magnetically levitated elevator system, the rope and the mechanical guiding can be replaced by a linear drive and a magnetic guiding, respectively. The power supply for on-board components has to be realized contactless, as well. Hereby benefits such as wearless operation of the cabin can be augmented. This paper introduces an inductive energy transmission along the shaft with segmented primary conductors and an e-shaped actuator, yielding the secondary winding.

Contents

1 Introduction

Electromagnetically levitated vehicles require a contactless power supply (CPS) to overcome the air gap between a fixed guide way and the moving part without sliding contacts or traveling cables. Hereby their benefits e.g. wearless operation, are augmented. Fast moving vehicles, e.g. maglev trains are able to consume power via harmonics induced by the propulsion device mounted to the guide way [12]. A slow moving elevator requires a separate transmission system.

At the Institute of Electrical Machines (IEM) a ropeless elevator test bench with a linear drive and electromagnetic guiding is built. The linear drive is realized by two long stator permanent magnet synchronous motors diagonally placed on the elevator shaft [16]. An air gap winding is applied to eliminate strong normal forces. On the moving part, the cabin, only permanent magnets need to be attached. The guiding system consists of four ω-actuators with two coils on each actuator [14] using a degree of freedom (DOF) control [9] for the translational and rotatory DOF of the elevator car. The design and control of the MGS are described in

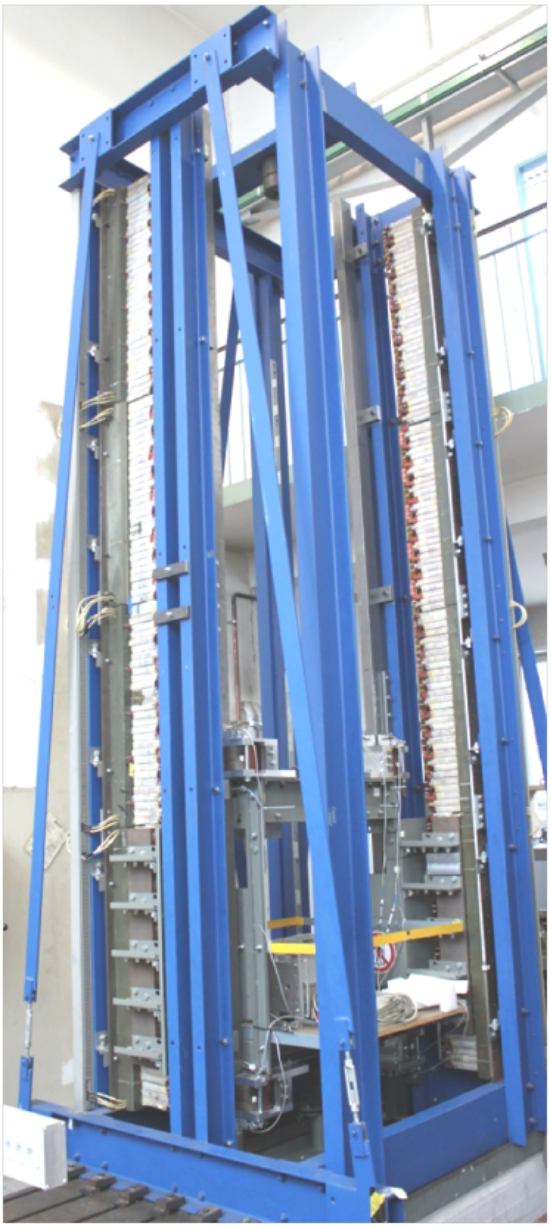

Figure 1: Ropeless elevator testbench.

detail in [4]. Figure 1 shows a photograph of the test bench.

Previous studies to minimize both, cost and space are based on an integrated solution of guiding and power transmission [17, 3]. A contactless power transmission at discrete places, i.e. the floors of a skyscraper, charging an on-board battery is shown in [2]. The topology

presented in this paper, is focused on a continuous energy transmission, based on segmented primary conductors and a secondary actuator mounted on the elevator cabin. Due to the air gap, an operation at high frequency is required.

2 Design process

The CPS has to transfer an electric power of 200 W across an air gap of 3 mm length to supply the on-board components such as magnetic guiding system or the cabin light and communication system. The design process of the transmission path is divided into the following chapters. First a characterization of the utilized soft ferrite material is presented. The electromagnetic design is shown, analytic and numeric calculations are presented. The design of the reactive power compensation finishes the process.

2.1 Material characterization

The actuator is designed for energy transmission only. The actuator should consists of a soft ferrite ceramic, due to its low eddy current losses. Therefore **Manifer (Mf) 102** from TRIDELTA Weichferrite GmbH [20] is used. To identify the electromagnetic parameters of this material, two identical u-shaped probes are wound with coils and measured at the core tester of a material test bench at the institute.

Inductive transmission systems normally operate in a high frequency region from 10 kHz up to several hundred kHz [5]. The induced voltage on the secondary is directly proportional the the operation frequency [21]. With rising frequency the diameter of magnetic flux guiding yokes and the size of additional filter components decreases, as well [8]. On the one hand the deliverable power is proportional to the frequency, on the other hand material and switching losses increase with the frequency, as well [13]. To determine the operation frequency of the power supply, the specific losses of the material are measured. Since the audible region of the human ear is approximately from 20 Hz to 20 kHz, the measurement is performed from 20 kHz to 30 kHz. Hereby the amplitude of the flux density is varied as well. Figure 2 depicts the specific material losses with respect to the frequency at different flux densities. It can be seen that the dependency of the flux density is higher than the dependency of the frequency. A maximal flux density of 0,1 T is defined to minimize core losses and an operation frequency of 25 kHz is chosen regarding to switching losses of power electronic components. Table I shows the magnetic material parameter at this working point.

Specific losses	$1,73 W/kg$
Relative permeability	3398

Table 1: Parameters of the soft ferrite at 25 kHz and 0,1 T.

2.2 Topology of the transmission path

After material characterization the electromagnetic design of the transmission path is done. By analytic magnetic circuit calculations various topologies of primary and secondary conductor arrangements in combination with different actuators (U-, E-, C-core) are analyzed regarding

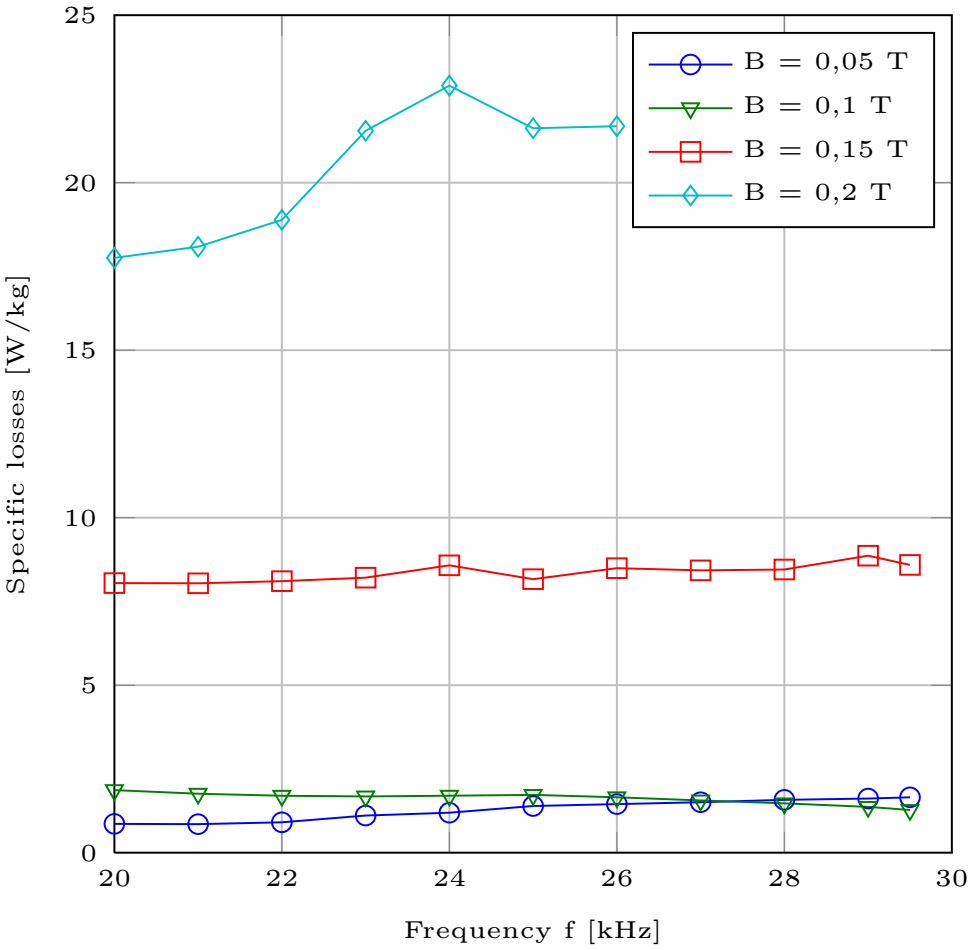

Figure 2: Specific losses with respect to frequency and flux density.

their applicability for a segmented inductive power transmission. The final design is configured using numerical finite element methods.

In figure 3 a design study based on [10, 19] for continuous CPS is presented. The primary winding consists of four parallel conductors, placed at the elevator shaft in segments. The secondary winding is wound in three coils on an e-shaped actuator. This e-shaped actuator with the secondary coils is placed at the elevator cabin. The choice of the actuator shape is mainly influenced by the primary winding configuration and the possibility of segmentation. By using an e-shape, the amount of primary conductors can be even-numbered (a pair of conductors forward and backward). With u-shaped actuators, one or three conductors systems, are required [18]. Furthermore the u-shape enables a segmentation of the primary conductors. Without collision with the actuator, the primary conductors can be connected backwards (compare figure 5). Regarding the ω-actuator [2], this is not possible.

The geometry of the actuator is determined by analytic calculation and finite element com-

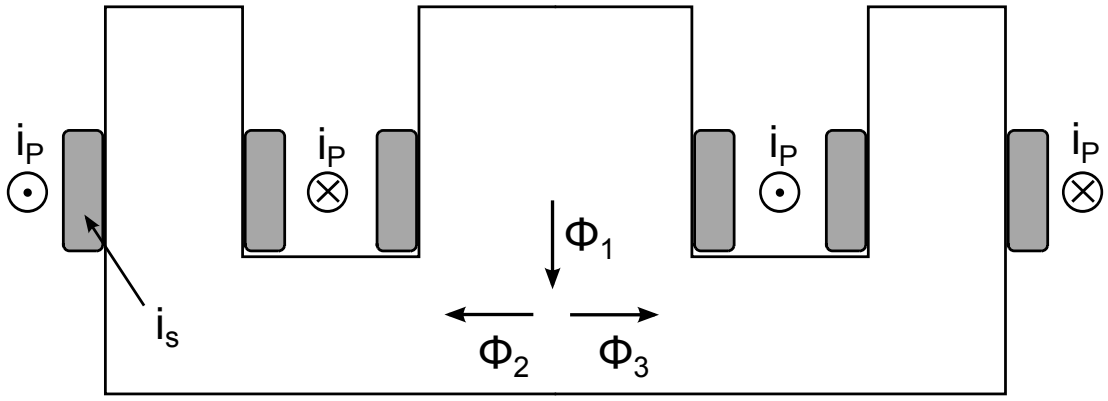

Figure 3: Topology of the transmission path.

putation. The design process is analog the methods presented in [2] for the u-shaped actuators.

The air gap between primary and secondary winding is 3 mm, which is the air gap distance of the linear guiding as well [4].

Since the winding number of primary conductors has to be small, due to mechanical stability reasons, the required MMF can only be achieved by a high primary current. To limit the diameter of the primary conductors due to cost and space requirements, the maximal primary current is limited to $\hat{i}_p = 50A$. Regarding a conductor cross section of 5 mm^2 and a transmission frequency of 25 kHz, the primary conductors have to be fabricated of litz wire. Hereby Skin- and Proximity effect can be suppressed [11].

The number of primary windings is chosen to $N_1 = 3$, to achieve the required flux density within the actuator yoke, for a power transmission of 200 W. Two primary coils are built by the two left and right conductors, respectively. One segment consists of these coils and the distance to the next segment is 10 mm. The primary current I_p circulates in the primary conductors. The orientation is defined in figure 3.

By three dimensional finite element simulation the magnetic circuit of the e-shaped actuator is analyzed. Figure 4 depicts the vectorial flux density in the yoke, generated by the primary conductors with $\hat{i}_p = 50A$. The magnetic flux penetrates the yoke and voltages are induced in the three secondary coils. Due to the high permeability of the soft ferrite, the magnetic flux density is much higher within the yoke compared to the surrounding air. A flux guiding at the shaft side is not regarded, here. A magnetic return path fabricated of soft ferrite ceramic would enhance the flux guiding, further. Such a return yoke has to be constructed over the whole shaft length, which means enormous costs and is thereby not efficient.

3 Simulation of the transmission path

To analyze the operational behavior of the transmission path, simulation at various position of the e-actuator in combination with the primary conductors are carried out. Furthermore the length of the primary conductors is varied. In figure 5 the magnetic flux density in the actuator

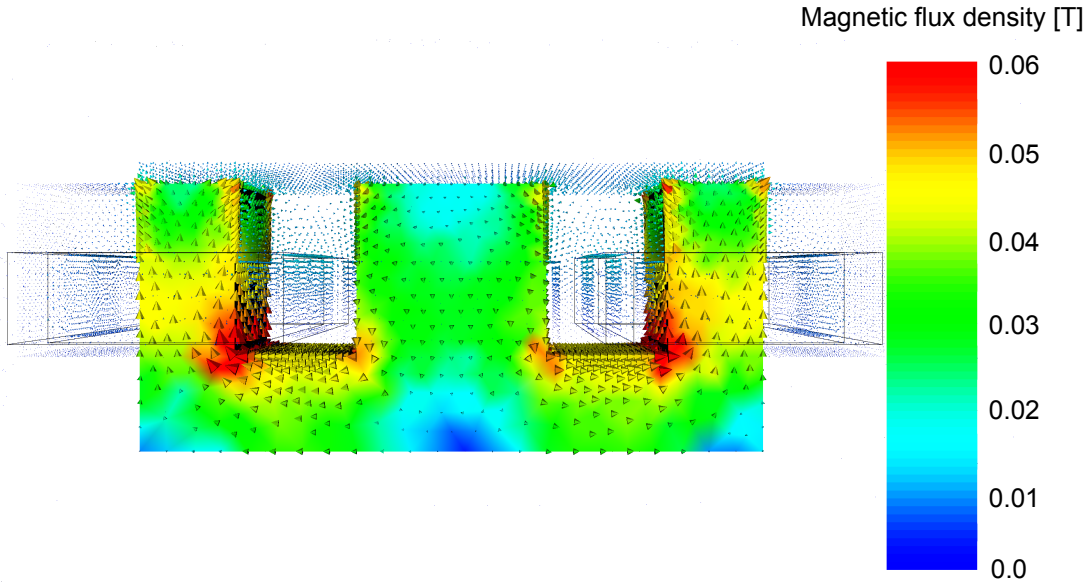

Figure 4: Magnetic flux density in the yoke of the e-shaped actuator.

yoke is presented at a primary current of $\hat{i} = 50A$, which is the nominal operation of the CPS. Due to the segmentation of the primary coil, the flux density distribution in the actuator varies during the ride of the cabin.

In the figure the flux density distribution in the actuator is shown at two different places. The first is at the center of the primary conductors, the second position is at the center of segmentation. There is a strong decrease of the amplitude of the flux density at the segmentation. To analyze the effects of the segmentation, regarding the energy transmission capability, inductance matrices are extracted at discrete position.

The CPS is modeled using a Π-equivalent circuit with self and mutual inductances, winding resistances and a parallel resistance describing the core losses. The following differential equation system characterizes the transmission path:

$$\begin{pmatrix} u_p \\ u_s \end{pmatrix} = \begin{pmatrix} R_p & 0 \\ 0 & R_s \end{pmatrix} \begin{pmatrix} i_p \\ i_s \end{pmatrix} + \partial_t \begin{pmatrix} \Psi_p \\ \Psi_s \end{pmatrix} \tag{1}$$

with the winding resistances $R_{p,s}$. The time-derivative of the flux linkages is given by:

$$\partial_t \begin{pmatrix} \Psi_p \\ \Psi_s \end{pmatrix} = \partial_{\mathbf{i}} \begin{pmatrix} \Psi_p \\ \Psi_s \end{pmatrix} \cdot \partial_t \begin{pmatrix} i_p \\ i_s \end{pmatrix}. \tag{2}$$

Regarding the operation of the considered CPS system the soft ferrite is not saturated. Therefore the derivative $\partial_{\mathbf{i}} \boldsymbol{\Psi}$ is constant, this yields:

$$\partial_{\mathbf{i}} \begin{pmatrix} \Psi_p \\ \Psi_s \end{pmatrix} = \mathbf{L} = \begin{pmatrix} L_p & -M \\ -M & L_s \end{pmatrix}. \tag{3}$$

L is the inductance matrix including primary and secondary self inductances and the mutual inductances.

The lumped parameter of the continuous CPS are shown in table 2.

Position $[mm]$	$L_p[\mu H]$	$L_s[\mu H]$	$M[\mu H]$	k
Center of primary coil	4,18	42,86	7,28	0,544
35	4,11	42,87	7,01	0,528
30	4,01	42,88	6,56	0,5
25	3,88	42,88	5,93	0,46
20	3,74	42,88	5,18	0,409
15	3,6	42,87	4,41	0,355
10	3,45	42,87	3,75	0,308
Center of segmentation	3,32	42,88	3,28	0,275

Table 2: Parameter of the continuous transmission path.

From simulation an inductance per unit length of $L'_p \approx 12,5\mu H/m$ for the primary conductors is determined. With rising length of the primary conductors, the leakage increases as well an the magnetic coupling of the coils decreases [15]. From simulation it can be further concluded, that the secondary inductance is constant ($L_s \approx 42,88\mu H$). The mutual inductance M varies with the position of the actuator. The magnetic coupling can be characterized by the coupling coefficient,

$$k = \frac{M}{\sqrt{L_s \cdot L_p}}. \tag{4}$$

In contrast to the model of transformers, and due to the relative large air gap, the coupling coefficient of contactless power supply systems is much smaller.

In figure 6 the variation of the mutual inductance M and the coupling coefficient k during a ride from the center of the primary conductor to the center of segmentation is depicted. It can be seen, that the magnetic coupling at the segmentation is least. When the e-actuator is driven to the center of the primary coil, the magnetic coupling increases.

4 Reactive power compensation

Without reactive power compensation the maximum transmittable power equals:

$$P_{max} = U_{s,oc}^2 \cdot \frac{R_{Load}}{R_{Load}^2 + (\omega \text{Ł}_s)^2} \tag{5}$$

Where $U_{s,oc}$ is the open circuit voltage of the secondary winding and R_{Load} is a resistance summarizing a diode rectifier and a battery storage. Various compensation topologies are discussed in literature [21]. Four possible reactive power compensation topologies are compared using the circuit simulator PLECS [1]. The simulation results are summarized in table 3.

For all cases the primary conductor current $\hat{i} = 50A$. The topologies with serial compensated primary require a too large input current, which corresponds to the primary current. The current source, i.e. an power electronic converter with an output filter, must be able to conduct this high current. This means it has to be overdimensioned and additional ohmic losses occur

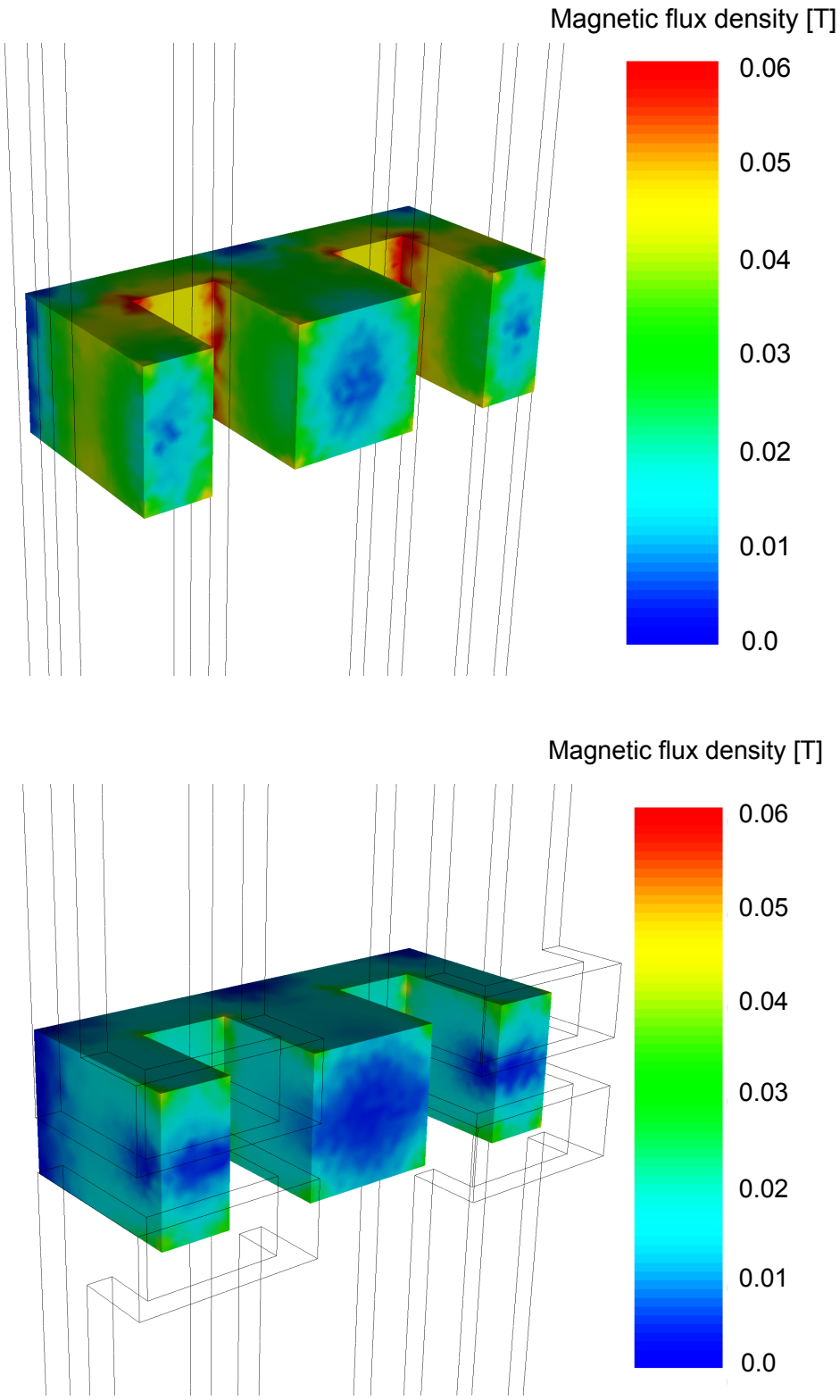

Figure 5: Magnetic flux density at different positions of the actuator.

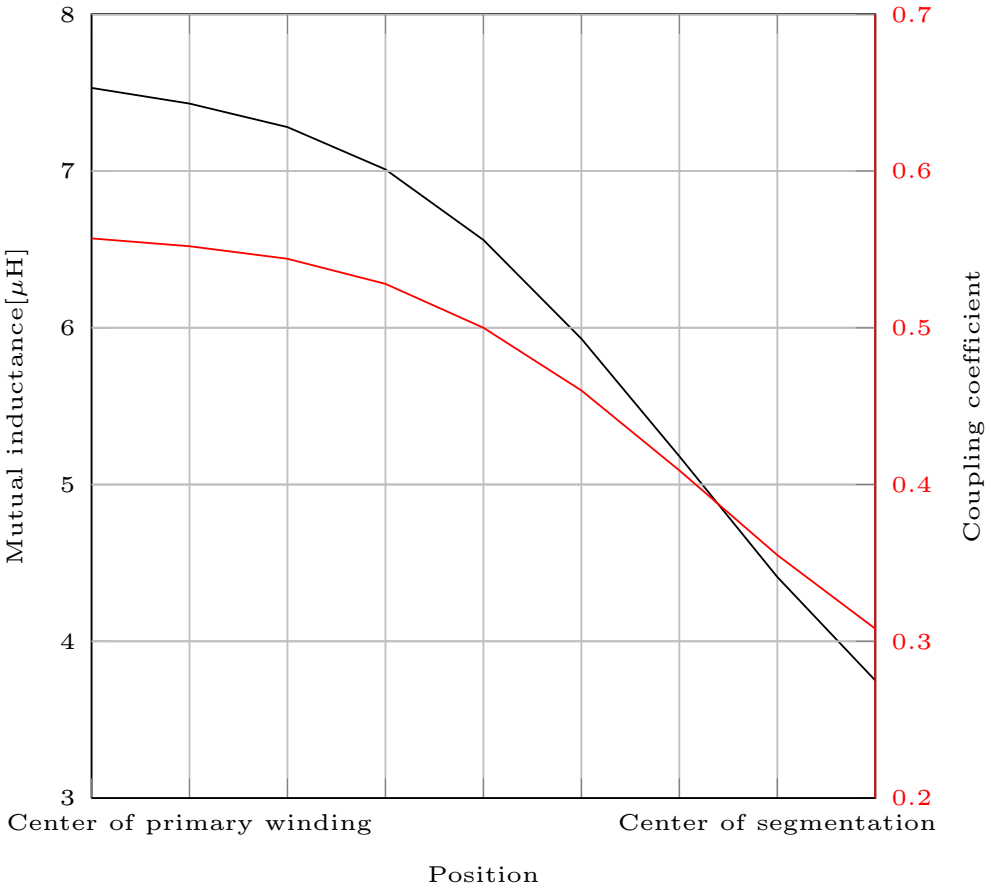

Figure 6: Variation of mutual inductance and coupling coefficient.

in the supply conductors.

The topologies with parallel compensated primary require approximately half of the input current to feed a primary current of $\hat{i} = 50A$. The resonant circuit of primary inductance and compensation capacitance amplifies the input current [7]. Moreover the parallel-serial (PS) topology has the highest efficiency and offers the highest transmittable power. Due to these considerations the PS-topology is chosen.

In figure 7 the efficiency of a segmented transmission path is shown. Here the effects of the segmentation in terms of efficiency can be seen (compare section 3). At the center of segmentation, the efficiency decreases to 28%. Hence the elevator cabin should drive through the segmentation fast. The segmentation must not be placed at the vertical stop station of the elevator shaft at each floor of the building.

Topology	U_{in} $[V]$	I_{in} $[A]$	U_{out} $[V]$	I_{out} $[A]$	P_{out} $[W]$	η [%]
SS	11,4	35,34	43,28	8,66	374,6	92,3
PS	23,39	17,23	43,35	8,67	375,9	93,3
SP	6,68	35,35	32,42	6,48	210,2	89,1
PP	14,11	16,74	32,37	6,47	209,6	88,7

Table 3: Simulation of the continuous transmission path.

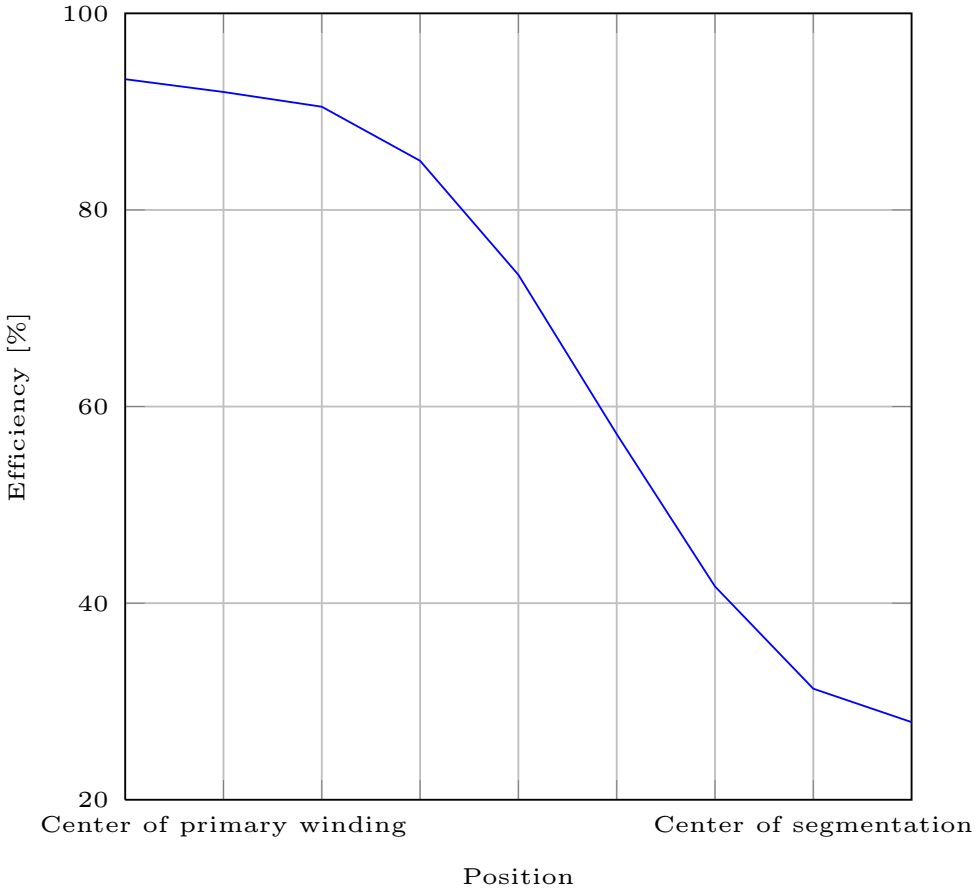

Figure 7: Efficiency of the CPS at different actuator positions.

5 Measurement results

To verify the design process, a segment of the CPS with a length of approximately 30 cm is built on a test bench. The e-shaped actuator is constructed from two identical u-shaped actuators fabricated from **Manifer (Mf) 102**, which are glued together on their lateral yokes. The three secondary coils are wound in series on the three yokes of the e-actuator. The primary conductor is fabricated from HF litz wire. It consists of several hundred twisted and insulated single conductors, which are connected in a solder bath at the end of the litz wire. This structure reduces Skin and Proximity effect. The conductors are positioned in three layers within a cable

trunking and fixed on a wooden plate to eliminated eddy currents in the supporting structure. Figure 8 depicts the measurement setup.

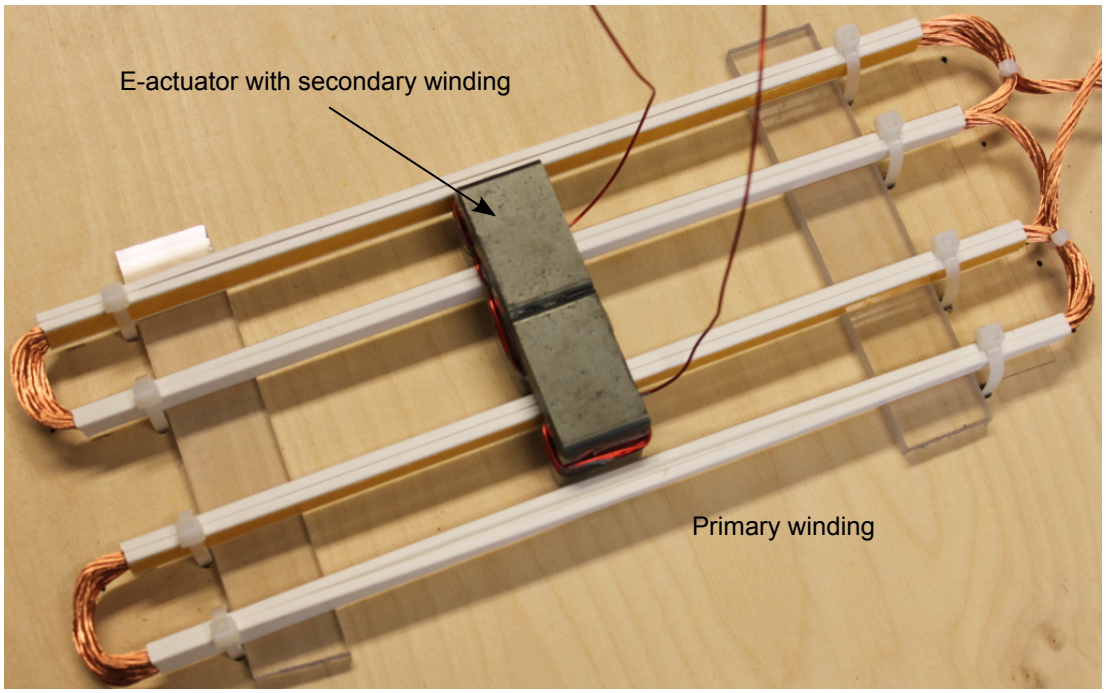

Figure 8: Prototype pf the continuous transmission path.

5.1 Parameter identification

From no-load measurement the elements of the inductance matrix are measured. The simulated and measured values are compared in table 4.

Inductance	simulation $[\mu H]$	measurement $[\mu H]$	deviation [%]
L_p	6,63	8,3	20,1
L_s	42,88	54,1	20,7
M	7,89	7,95	1

Table 4: Simulation of the continuous transmission path.

There is a very good correlation between the mutual inductance M between simulation and measurement. The self inductances L_p and L_s deviate stronger at the test bench compared to simulation. The simplifications in the modeling process explain these deviation. Not all supply conductors, or cable connections at the test built up, are modeled in simulation. Wherever the litz wire is not modeled using single conductors in simulation. Therefore the measured inductances are slightly higher compared to simulation. In the following section the power transmission capability is considered with the measured parameter of the CPS.

5.2 Operation of the prototype

The transmission path is built using parallel-serial compensation and connected to a load resistance of 5,2 Ω. A linear amplifier is used for the current source. Table 5 summarizes the lumped parameter of the transmission path. An additional input resistance of 11 Ω is connected in series to the CPS, hereby the input resistance is increased an the THD of the input current is reduced. Table 6 shows the measured operation points. Due to limitations of electrical components, the transmittable power is limited to < 100 W. The transmission path itself, can supply a power of 200 W (compare chapter 3).

Starting resistor R_{start}	11Ω
Winding resistance R_p	$17,1m\Omega$
Winding resistance R_s	$67,5m\Omega$
Primary capacitance C_p	$4,75\mu F$
Secondary capacitance C_s	$0,76\mu F$
Load resistance R_{load}	$5,2\Omega$

Table 5: Parameter of the continuous transmission path.

U_{in} $[V]$	I_{in} $[A]$	φ [°]	U_{out} $[V]$	I_{out} $[A]$	P_{out} $[W]$	η [%]
7,69	1,89	20	7,92	1,53	12,08	83,2
11,34	2,79	20	11,66	2,24	26,17	82,8
14,85	3,7	20	15,35	2,97	45,53	82,9
18,7	4,66	20	19,33	3,73	72	82,7

Table 6: Working points of the continuous transmission path.

From measurement it can be seen, that the reactive power compensation does not compensate the phase shift between voltage and current completely. The input current is delayed by 20° compared to the input voltage. An under-compensation occurs. Therewith the reactive power demand of the transmission path is increased. Hence the efficiency of the CPS decreases and the simulated efficiency is not matched completely. An adjustment of the compensation capacities is not feasible at the prototype of the CPS. The capacity values are in a region, where component tolerances and additional cable capacities have a strong influence.

Figures 9 and 10 depict the simulated and measured electric input and output quantities, respectively. The simulated voltages are higher when compared to the measured voltages. In simulation the linear amplifier is modeled as ideal current source with a parallel resistance. This simplification explains the deviation compared to measurement. The phase shift between the simulated and measured output currents can be explained by the non ideal reactive power compensation. The current in the secondary winding is generated by the induced voltage, which is in phase with the voltage in the primary coil. The primary voltage is 20° ahead compared to the primary current. Hence the simulated and measured output currents are phase shifted by this value. Considering the referred deviations, the modeling of the CPS matches with the measurement results and the design process is verified.

This topology provides as continuous contactless power supply with high efficiency for a ropeless elevator. Due to the segmentation of the primary conductors, the losses in the primary conductors can be reduced significantly. Furthermore additional secondary actuators can be

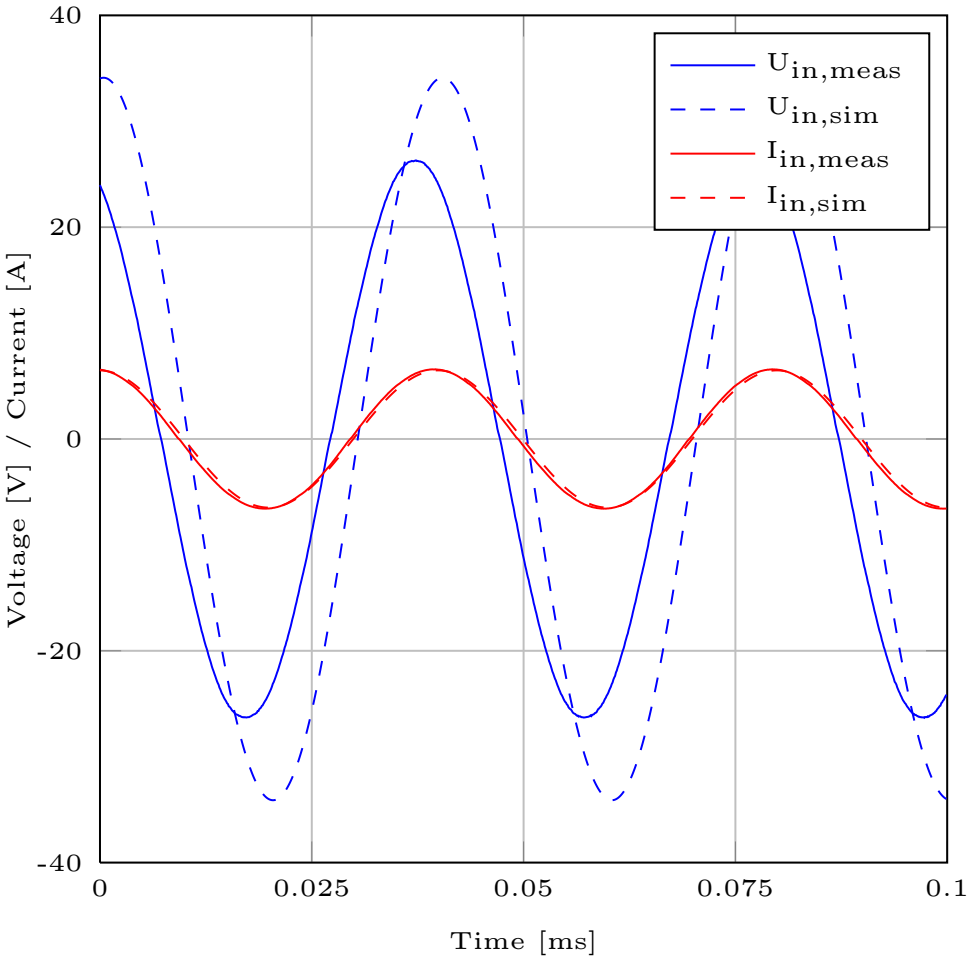

Figure 9: Electric input quantities of the CPS.

operated without interfering the primary coil. [6, 22]. This scenario occurs, when multiple cabins operate in a single shaft.

6 Conclusions

In this paper a segmented CPS for a vertical transportation vehicle is introduced. The primary consists of segmented litz wire and the secondary is mounted on an e-shaped actuator at the elevator car. The design process is described, beginning with material characterization, magnetic circuit design and reactive power compensation. Parameter extraction is done using finite element method and analytic models. A prototype is built and measurement results verify the design methodology. The proposed topology offers an efficient contactless power transmission for a ropeless elevator system.

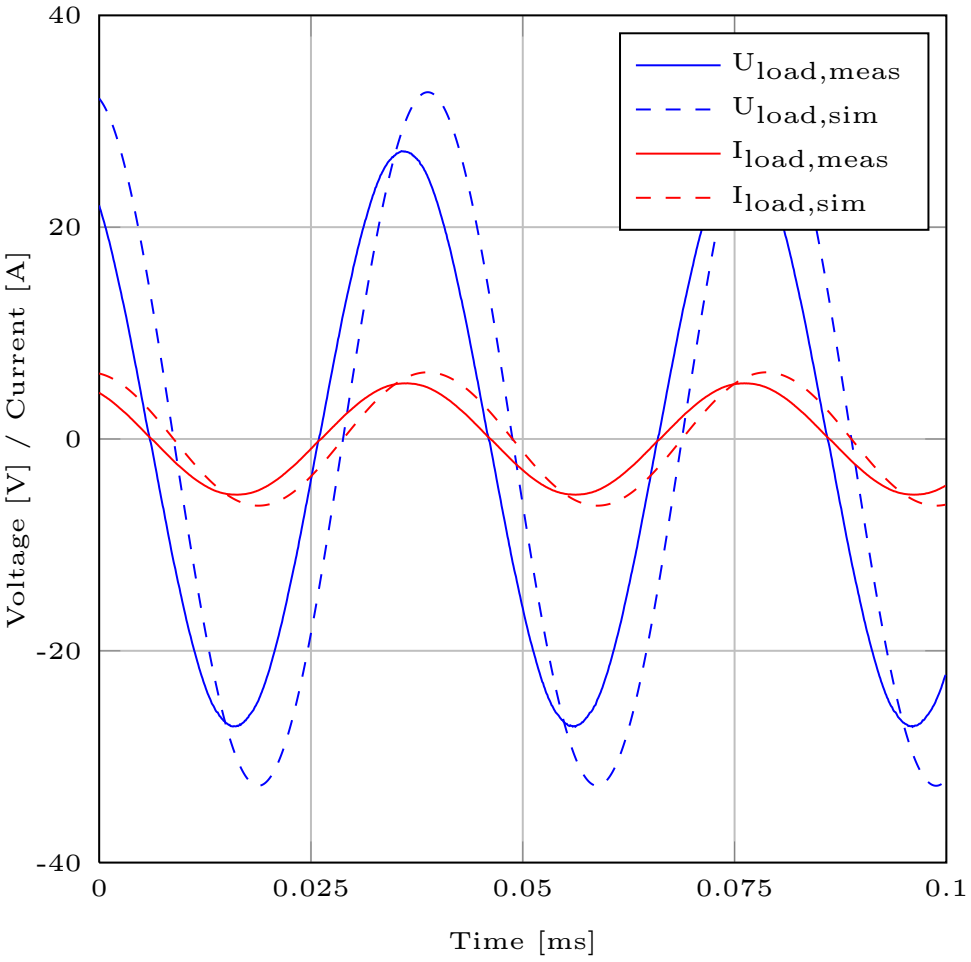

Figure 10: Electric output quantities of the CPS.

References

[1] J.H. Allmeling and W.P. Hammer. Plecs-piece-wise linear electrical circuit simulation for simulink. In *Power Electronics and Drive Systems, 1999. PEDS '99. Proceedings of the IEEE 1999 International Conference on*, volume 1, pages 355 –360 vol.1, 1999.

[2] R. Appunn, A. K. Putri, and K. Hameyer. Design of a contactless power supply for magnetically levitated elevator systems integrated into the guide rail. In *Linear Drives for Industry Applications, 2013. LDIA. International Symposion on*, 2013.

[3] R. Appunn, B. Riemer, and K. Hameyer. Contactless power supply for magnetically levitated elevator systems. In *Electrical Machines (ICEM), 2012 XXth International Conference on*, pages 600–605, Sept 2012.

[4] R. Appunn, B. Schmülling, and K. Hameyer. Electromagnetic Guiding of Vertical Transportation Vehicles: Experimental Evaluation. *IEEE Trans. on Industrial Electronics*, 57(1):335–343, January 2010.

[5] J.M. Barnard, J.A. Ferreira, and J.D. Van Wyk. Sliding transformers for linear contactless power

delivery. *Industrial Electronics, IEEE Transactions on*, 44(6):774–779, 1997.

[6] J.T. Boys, G.A. Covic, and A.W. Green. Stability and control of inductively coupled power transfer systems. *Electric Power Applications, IEE Proceedings* -, 147(1):37 –43, January 2000.

[7] M. Budhia, G. Covic, and J. Boys. A new ipt magnetic coupler for electric vehicle charging systems. In *IECON 2010 - 36th Annual Conference on IEEE Industrial Electronics Society*, pages 2487–2492, 2010.

[8] M. Dockhorn, D. Kurschner, and R. Mecke. Contactless power transmission with new secondary converter topology. In *Power Electronics and Motion Control Conference, 2008. EPE-PEMC 2008. 13th*, pages 1734–1739, 2008.

[9] A. S. Ghersin and R. S. Sánchez Peña. LPV Control of a 6-DOF Vehicle. *IEEE Transactions on Control Systems Technology*, 10(6):883–887, November 2002.

[10] A. W. Green and J. T. Boys. 10 khz inductively coupled power transfer-concept and control. In *Power Electronics and Variable-Speed Drives, 1994. Fifth International Conference on*, pages 694–699, 1994.

[11] D. Kurschner and C. Rathge. Integrated contactless power transmission systems with high positioning flexibility. In *Power Electronics and Motion Control Conference, 2008. EPE-PEMC 2008. 13th*, pages 1696–1703, 2008.

[12] J.-Y. Lee, I.-J. Lee, J.-W. Kim, J.-H. Chang, D.-H. Kang, S.-U. Chung, and J.-P. Hong. Contactless power transfer system combined with linear electric machine. In *Electrical Machines and Systems, 2007. ICEMS. International Conference on*, pages 1544 –1548, 2007.

[13] N. Mohan, T. M. Undeland, and W. P. Robbins. *Power Electronics - Converters, Applications and Design*. John Wiley & Sons, New York, 2003.

[14] M. Morishita and M. Akashi. Electromagnetic non-contact guide system for elevator cars. In *The Third International Symposium on Linear Drives for Industry Applications*, pages 416–419, Nagano, Japan, October 2001. LDIA.

[15] M. Nishimura, A. Kawamura, G. Kuroda, Chi Zhu, and E.K. Sato. High efficient contact-less power transmission system for the high speed trains. In *Power Electronics Specialists Conference, 2005. PESC '05. IEEE 36th*, pages 547–553, 2005.

[16] M. Platen and G. Henneberger. Examination of leakage and end effects in a linear synchronous motor for vertical transportation by means of finite element computation. *IEEE Transactions on Magnetics*, 37(5):3640–3643, September 2001.

[17] B. Schmülling and K. Hameyer. PowerTRACE - a Novel Power Transmission and Actuator Entity. In *20th International Conference on Magnetically Levitated Systems and Linear Drives, MAGLEV*, pages 15–18, San Diego, USA, December 2008.

[18] P. Sergeant and A. Van den Bossche. Inductive coupler for contactless power transmission. *Electric Power Applications, IET*, 2(1):1–7, 2008.

[19] B.-M. Song, R. Kratz, and S. Gurol. Contactless inductive power pickup system for maglev applications. In *Industry Applications Conference, 2002. 37th IAS Annual Meeting. Conference Record of the*, volume 3, pages 1586–1591 vol.3, 2002.

[20] TRIDELTA Weichferrite GmbH. Manifer-werkstoffe fr hohe aussteuerungen. http://www.tridelta.de, December 2012.

[21] C.-S. Wang, O.H. Stielau, and G.A. Covic. Design considerations for a contactless electric vehicle battery charger. *Industrial Electronics, IEEE Transactions on*, 52(5):1308 – 1314, October 2005.

[22] D. Wesemann, S. Witte, and J.-S. Michels. Effects of multiple loads in a contactless, inductively coupled linear power transfer system. In *Electrical and Electronics Engineering, 2009. ELECO 2009. International Conference on*, pages I–54–I–59, 2009.